Electron localization in recrystallized models of the Ge₂Sb₂Te₅ phase-change memory material

Konstantinos Konstantinou [1,*] Felix C. Mocanu [2] and Jaakko Akola [1,3]

[1]*Computational Physics Laboratory, Faculty of Engineering and Natural Sciences, Tampere University, Tampere FI-33014, Finland*
[2]*Laboratoire de Physique de l'Ecole Normale Supérieure, ENS,*
Université PSL, CNRS, Sorbonne Université, Université de Paris, Paris F-75005, France
[3]*Department of Physics, Norwegian University of Science and Technology (NTNU), Trondheim NO-7491, Norway*

Understanding the relation between the structural disorder in the atomic geometry of the recrystallized state of phase-change memory materials and the localized states in the electronic structure is necessary not only for technological advances, but also essential to achieve a fundamental understanding of these materials. In this computational study, hybrid density-functional theory simulations are employed to ascertain the impact of antisite defects on the spatial localization of the electronic states in the bottom of the conduction band in recrystallized models of the prototypical phase-change material Ge₂Sb₂Te₅. Te-Te homopolar bonds are the local defective atomic environments mainly responsible for the electron localization of the conduction-band-edge states in the simulated structures, while Sb-Te chains can also induce spatial localization. Unoccupied defect-related electronic states can emerge in the band gap during a crystallization event, while Sb-Sb homopolar bonds have been identified in the defect environment of a deep localized state.

I. INTRODUCTION

Phase-change memory (PCM) materials exhibit a pronounced difference in optical and electronic properties between the amorphous and crystalline states, which, in principle, makes them appealing for storage applications by encoding digital binary data as structural changes in the material [1]. Nowadays, PCM materials are considered as a contender for next-generation nonvolatile electronic-memory technology (a replacement for silicon-based flash memory) and for new storage-class memory devices, as well as for all-photonic neuromorphic computing architectures [2]. Moreover, phase-change random-access memory (PCRAM) is a novel technology that is currently used in the Mircon-Intel Optane^{TM} solid-state memory device.

The function of PCRAM devices is governed by the application of voltage (laser) pulses, which switch the chalcogenide memory material due to Joule heating, very rapidly ($\approx$ns) and, reversibly, between metastable structural states; a degenerate semiconducting, electrically conductive crystalline state (the "1-bit") and a semiconducting, electrically resistive amorphous state (the "0-bit") [1,2]. The canonical composition Ge₂Sb₂Te₅ (GST-225), on the pseudobinary GeTe-Sb₂Te₃ tie line, is utilized as the core material for PCRAM programming [1,2].

The metastable crystalline state of GST-225, which is formed upon rapid crystallization during the phase-change transformation inside the PCRAM cell, has a cubic rock-salt (NaCl), cation-vacancy-containing atomic structure [3]. In particular, the cationlike sublattice is occupied by Ge and Sb atoms, and atomic vacancies randomly distributed within the crystal structure, while the anionlike sublattice is taken by Te atoms. The disordered rock-salt crystalline structure of GST-225 alloys was proposed by Yamada and Matsunaga based on x-ray diffraction data [4,5], while this view was also supported by transmission electron microscopy experiments [6,7], as well as by *ab initio* molecular-dynamics (MD) simulations of the crystallization process [8–12]. It is noted that the stable crystalline phase of GST-225 is a hexagonal structure, which is made of atomic blocks of seven and nine alternating Ge/Sb and Te layers, respectively, held together by Van der Waals forces [13–15].

Structural disorder in amorphous (glassy) materials serves as a natural cause for the formation of spatially localized defect electronic states in the band gap [16]. It has been reported from experimental studies [17] and atomistic simulations [18–22] that several localized unoccupied and occupied electronic states exist in the vicinity of the band gap in amorphous PCM materials.

Although the disorder-induced electron localization prevails in amorphous semiconductors, it has also been observed to have a significant impact on the rock-salt crystalline structure of PCM materials. The statistical distribution of the high-concentration atomic vacancies, together with the Ge and Sb atoms, on the cationlike sublattice corresponds to the main component of disorder in crystalline GST-225, which was thought that it can give rise to the localization of the electrons [3]. Electron localization due to this type of disorder has been identified by low-temperature transport experiments [23], while density-functional theory (DFT) simulations in models of disordered crystals indicated that the fluctuations in the (randomly or manually generated) distribution of atomic vacancies and the consequent formation of vacancy clusters

*konstantinos.konstantinou@tuni.fi

within the structure can induce localization of the electronic states near the valence-band edge [24]. Atomic displacements away from the ideal rock-salt lattice sites were found to be insignificant for the electron localization in GST-225, while it was shown that excess vacancies can shift the Fermi level towards lower valence-band energies, but not away from the localization region [24].

Fractions of antisite defects were found in recrystallized GST-225 models, obtained by DFT-MD simulations [8–12,25], which led to the generation of Te-Te and Ge(Sb)-Ge(Sb) homopolar bonds within the recrystallized structures. Hence, these antisite defects increase the compositional disorder, which, in turn, can influence the electronic properties of the material. Xu *et al.* in a study of crystalline $Ge_1Sb_2Te_4$ under high pressure using DFT-MD simulations reported that the electronic states near the bottom of the conduction band are localized around pairwise antisite atoms, highlighting a disorder-induced electron localization triggered by pressure [26]. More recently, large-scale ($\approx$1000 atoms) DFT-MD crystallization simulations in a model of amorphous $Ge_1Sb_2Te_4$ showed that Te antisite defects and Sb-Te chains can lead to electron localization of conduction-band-edge states in the recrystallized structure of the material [27]. It is noted that in these studies the localization properties of the occupied electronic states at the top of the valence band were found to be unaffected by the presence of the antisite defects inside the crystalline structure [26,27].

The structural aspect of disorder and the contributions of the different types of defects that are responsible for spatial localization of the electronic states are very difficult to be disentangled by experimental measurements [3]. In this study, we aim to achieve a fundamental understanding, at the atomistic level, of the connection between atomic structure and electronic properties of the recrystallized state in PCRAM devices. We utilize DFT calculations using nonlocal exchange-correlation functionals to explore the spatial localization and atomic character of defect electronic states in recrystallized models of the GST-225 PCM material. We provide a picture of the interplay between the antisite defects and electron localization in the conduction-band-edge states of the modeled structures. Moreover, an investigation of the evolution of the electronic structure during recrystallization is presented to study the generation of defects that take place during this process inside the memory cell.

II. COMPUTATIONAL METHODS

A. Model structures

Structures of 460 atoms from previous long-scale DFT-MD crystallization simulations of amorphous GST-225 [9–11] have been used in this study to investigate the electronic structure of the recrystallized models with hybrid-DFT calculations, and to identify the nature of electron localization. In particular, the recrystallized structures obtained from two different simulations with an ordered history (i.e., by manually embedding a crystalline seed inside the initial amorphous network) were selected to gain an understanding about their electronic properties. Both these simulations were performed at 600 K; however, in one of them the crystalline seed was

not fixed during the crystallization process (model *M1*) [10], whereas in the other the inserted crystalline seed was kept fixed during the whole simulation (model *M2*) [9]. The final recrystallized structure from a similar simulation (with a fixed crystalline seed) performed at 700 K (model *M3*) [9] was also used here to extend our investigation about the electron localization in more diverse samples. In addition, three independent recrystallized models (*M4*, *M5,* and *M6*) obtained from crystallization simulations performed at 600 K and without any imposed structural constraints (before or during the simulations) [10] were used in this study to calculate their electronic properties. Moreover, nine configurations from the simulated crystallization trajectory of model *M5* were selected to examine the evolution of the electronic structure during the recrystallization process of the amorphous sample. The selected structures were the initial amorphous configuration ($t = 0$ ns), four intermediate configurations corresponding to the DFT-MD snapshots before a steplike density change, at 2.2, 3.4, 4.2, and 5.7 ns, and the final recrystallized geometry ($t = 7.1$ ns). In addition, three more configurations of the same density (snapshots at 4.6, 5, and 5.4 ns) were selected to examine further the formation of the deep unoccupied electronic states identified in the given model (*M5*). Details about these crystallization simulations can be found in Refs. [9–11].

As mentioned above, the metastable cubic rock-salt-like crystalline state of GST-225 is typically characterized by a Te-atom anionic sublattice and a cationic sublattice that is randomly occupied by Ge and Sb atoms, as well as by atomic vacancies. A representative model of this random crystalline structure can be obtained from the generation of a *special quasirandom structure* (SQS), which aims to mimic the physically most relevant radial correlation functions of the target configuration [28]. In this study, a simulated annealing protocol was used to optimize a putative 720-atom random alloy structure of GST-225 from an initial guess by swapping atoms around within the cation sublattice until the cluster vector resembles as closely as possible that of the target structure. It is noted that the Te sublattice was kept fixed during the Monte Carlo simulation. The implementation provided by the ICET library was utilized for this procedure [29,30]. The atomic geometry of the generated SQS model structure was then optimized with a hybrid-DFT calculation in the same way as the recrystallized models studied here in order to calculate its electronic structure and facilitate comparisons.

B. Electronic-structure calculations

DFT as implemented in the CP2K code was used to optimize the geometries of the model GST-225 structures and to calculate their electronic properties [31]. The CP2K code employs a mixed Gaussian basis set with an auxiliary plane-wave basis set to represent the electrons in the modeled system [32]. A molecularly optimized double-ζ valence-polarized (DZVP) Gaussian basis set was used for all atomic species [33], in conjunction with the Goedecker-Teter-Hutter (GTH) pseudopotential [34]. The plane-wave energy cutoff was set to 5440 eV (400 Ry). The range-separated hybrid PBE0 functional was used in all calculations [35]. The inclusion of the Hartree-Fock exchange offers a more credible description of the electronic structure and, especially, the localized
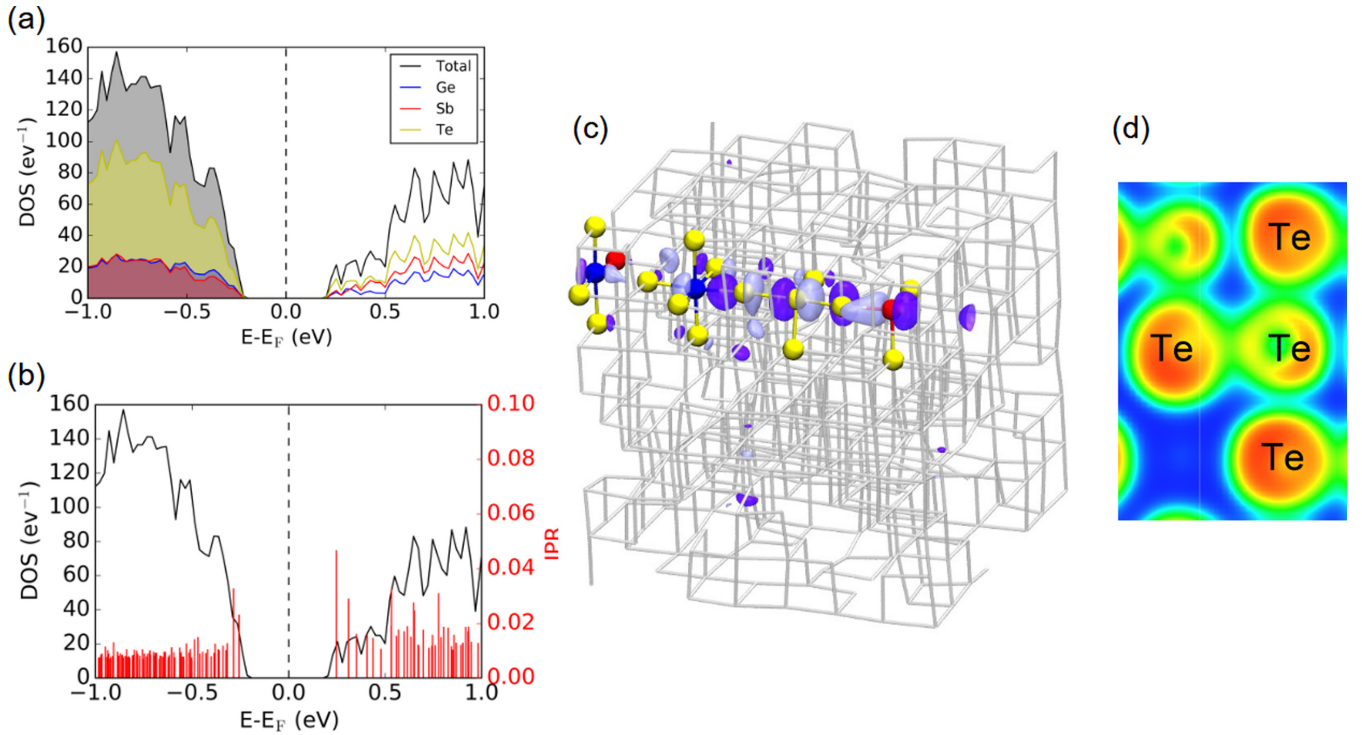
FIG. 1. (a) Total and partial electronic densities of states (DOS/PDOS) around the Fermi level of the recrystallized GST-225 model *M1*. (b) DOS (black solid line) of model *M1* and the corresponding inverse participation ratio (IPR) values for the Kohn-Sham orbitals (red spikes). (c) Atomic structure and molecular orbital of the localized conduction-band-minimum electronic state. Ge atoms are blue, Sb are red, and Te are yellow. The atomic bonds in the rest of the recrystallized structure are rendered as gray sticks. The purple and blue isosurfaces depict the molecular-orbital wave-function amplitude of the electronic state and are plotted with isovalues of $+0.02$ and $-0.02\ e\text{Å}^{-3}$, respectively. (d) 2D projection of the calculated electron-localization function (ELF) near the Te antisite defects that are associated with the spatial localization of the electronic state shown in (c).

electronic states that are potentially present in our simulated GST-225 structures [20,36]. A comparison between standard PBE and hybrid PBE0 functionals, for selected configurations of the simulated structures studied here, shows that the utilization of a hybrid functional results in a more accurate calculation of the band gap, as well as in a stronger spatial localization of the conduction-band-edge electronic states in the recrystallized models (see Figs. S1–S3 in [37]). The computational cost of hybrid-functional calculations was reduced by using the auxiliary density-matrix method (ADMM) [38]. The Broyden-Fletcher-Goldfarb-Shanno (BFGS) algorithm was applied in the geometry optimizations to minimize the total energy of the modeled systems with respect to the atomic coordinates. The convergence criterion for the forces on atoms of the current configuration in an iteration step was 0.023 eV Å^{-1} (4.5×10^{-4} Hartree bohrs^{-1}). Periodic-boundary conditions were enforced in all the calculations.

III. RESULTS AND DISCUSSION

A. Nature of electron localization

The total and partial electronic densities of states (DOS, PDOS, respectively) near the top of the valence band and the bottom of the conduction band of the recrystallized GST-225 model *M1* are shown in Fig. 1(a). The hybrid-DFT electronic-structure calculation results in a Kohn-Sham (KS) band gap of 0.5 eV for the relaxed ground state. The calculated value of the

band gap agrees very well with the experimentally reported value for the crystalline state of GST-225 [39,40]. The LUMO (lowest unoccupied molecular orbital) electronic state, at the bottom of the conduction band, is dominated by the contribution from Te-atom states with some contribution from Ge- and Sb-atom states as well. The degree of spatial localization of the LUMO state, as well as of each single-particle KS state in the electronic structure of the recrystallized model, can be examined quantitatively by calculating the inverse participation ratio (IPR). This method has been previously widely used to characterize the localization of vibrational and electronic states in amorphous and crystalline materials in several simulation studies [18,20,22,24,27,41–43]. The IPR spectrum near the valence- and conduction-band edges for the recrystallized GST-225 model *M1* is shown in Fig. 1(b). One can clearly observe that the LUMO corresponds to a fairly strongly localized state, with an IPR value of ≈ 0.05. In addition, the IPR analysis shows that a few more partially localized tail states appear at the band edges of this recrystallized model.

Direct inspection of the molecular orbital reveals the atomic environment that hosts the localized LUMO electronic state in the periodic cell of the recrystallized GST-225 model *M1* [Fig. 1(c)]. A Te-Te-Te three-atom chain corresponds to a local environment that is involved in the spatial localization of the LUMO state within the model structure. Moreover, the central Te atom of this configuration was found to be bonded to two more Te atoms. The presence of
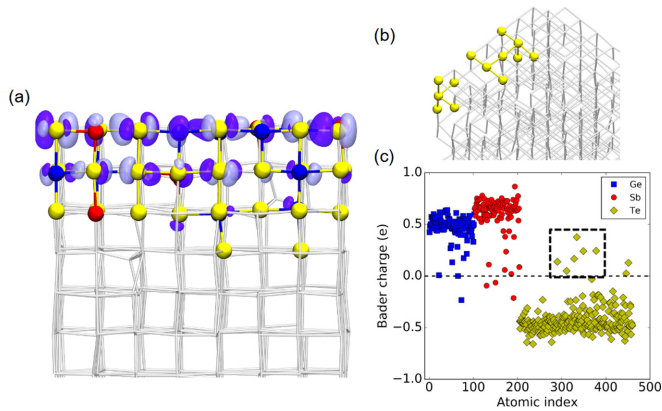
FIG. 2. (a) Molecular orbital and atomic structure of the electronic state at the bottom of the conduction band in the recrystallized GST-225 model *M2*. Color codes and representations for atomic species, bonds, and isosurfaces as in Fig. 1. (b) The group of Te-Te homopolar bonds (antisite defects) associated with the spatial localization of the electronic state shown in (a). (c) Bader ionic charge distributions of Ge, Sb, and Te atoms in the recrystallized model *M2*. Each point corresponds to an individual atom in the 460-atom GST-225 simulated structure. Some of the Te atoms from the structural pattern identified in (b) are shown inside the black dashed frame.
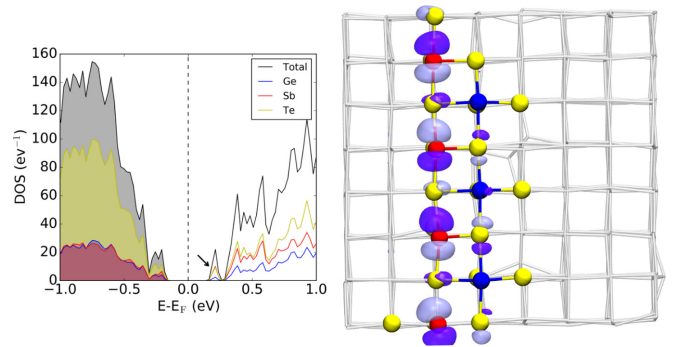

FIG. 3. Left panel: Total and partial electronic densities of states (DOS/PDOS) around the Fermi level of the recrystallized GST-225 model *M3*. Right panel: Molecular orbital and atomic geometry of the conduction-band-minimum electronic state (denoted with an arrow in the DOS). Color codes and representations for atomic species, bonds, and isosurfaces as in Fig. 1.

these Te-Te homopolar bonds in the atomic geometry of the LUMO highlights the significant contribution of the antisite defects to the electron localization of the conduction-band-edge state of the recrystallized model. One three-coordinated Sb atom and a six-coordinated Ge atom also contribute to the structural pattern that hosts the localized electronic state.

The electron-localization function (ELF) [44] can be used as a measurement that indicates the probability of finding electron pairs and it corresponds to an approach that has been previously employed to characterize the bonding in amorphous [20,21,45,46] and crystalline [47–49] structures. The calculated ELF for the recrystallized GST-225 model *M1* was projected in an optimal plane defined by the atomic environment that is associated with the spatial localization of the LUMO state in the model structure and the results are shown in Fig. 1(d). Values of the ELF close to unity are shown in red and highlight perfect electron localization (referring to perfect covalent bonding), whereas values close to zero are shown in blue and are indicative of very little or no electron localization (essentially no bonding) in that region of space [50]. A value of 0.5 (shown in green) corresponds to a delocalized ELF similar to that of the homogeneous electron gas [44], while any values between 0.5 and 1 denote varying degrees of covalent bonding [50]. Also, the red color around the marked atoms highlights their atomic valence shells.

Visualization of the molecular orbital for the LUMO electronic state in the recrystallized model *M2*, with a fixed crystalline seed throughout the simulation, is shown in Fig. 2(a). The spatial localization of the electronic state is more extended within the periodic cell of the simulated structure compared to that in recrystallized model *M1*. Nevertheless, it can be observed that a group of Te-Te homopolar bonds is involved again in the structural pattern that is respon-

sible for the spatial localization of the LUMO [Fig. 2(b)]. This highlights further the significant role of the Te antisite defects in the character of electron localization for conduction-band-minimum states in recrystallized models of GST-225.

A Bader-charge analysis was performed for the atomic species in the recrystallized GST-225 model *M2* to identify, from an electronic-structure-oriented perspective, the existence of homopolar bonds inside the simulated structure. The Bader ionic charges were computed from the converged total electronic charge density of the hybrid-DFT geometry optimization by using the scheme described in Ref. [51]. The distribution of the calculated Bader charges is shown in Fig. 2(c), while the average values for Ge, Sb, and Te atoms were found to be $0.47e$, $0.60e$, and $-0.42e$, respectively. For all atomic species, the distribution of ionic charges is rather narrow around the corresponding average value, which is a characteristic behavior of a crystallinelike structure. However, when data of the distribution tail towards zero this is indicative of the presence of homopolar bonds within the simulated structure. The results of the calculation show that some Te atoms have a positive Bader charge (as highlighted inside the black dashed frame), which are the specific Te atoms that participate in the structural motif [Figs. 2(a) and 2(b)] where the LUMO electronic state of the model structure *M2* is spatially localized.

The DOS/PDOS near the top of the valence band and the bottom of the conduction band of the recrystallized GST-225 model *M3*, obtained from a simulation at 700 K with a fixed crystalline seed, are shown in Fig. 3 (left). A KS band gap of 0.42 eV was derived for the relaxed ground state from the hybrid-DFT electronic-structure calculation, slightly smaller than that of the *M1* recrystallized structure at 600 K. Moreover, the contribution from Sb-atom states was found to be much more significant for the LUMO electronic state (highlighted with an arrow in the relevant DOS in Fig. 3), compared to that for model *M1*, suggesting a different character of electron localization at the bottom of the conduction band. The nature of spatial localization for the LUMO state in the recrystallized model *M3* can be examined by visualization of the molecular orbital of the electronic state, shown
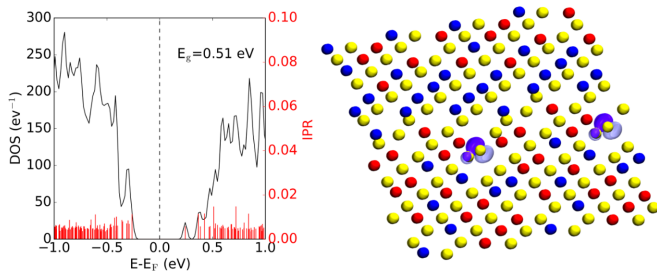
FIG. 4. Left panel: Total electronic density of states (DOS, black solid line) and the corresponding inverse participation ratio values for the Kohn-Sham orbitals (IPR, red spikes) near the top of the valence band and the bottom of the conduction band of the simulated special quasirandom crystalline structure (SQS) of GST-225. Right panel: Molecular orbital and atomic structure of the valence-band-maximum electronic state (HOMO). Color codes and representations for atomic species and isosurfaces as in Fig. 1.

in Fig. 3 (right). An Sb-Te-Sb-Te chain structure across the simulation cell serves as the geometric host of the localized conduction-band-edge state in the recrystallized model structure, revealing a different picture than the Te-Te homopolar bonds (antisite defects) observed in the other simulated structures (*M1* and *M2*).

The total DOS together with the IPR spectrum of the electronic states near the valence- and conduction-band edges for the SQS-generated crystalline structure of GST-225 are shown in Fig. 4 (left). The hybrid-DFT electronic-structure calculation results in a KS band gap of 0.51 eV for the relaxed ground state, which is in close agreement with the experimentally reported value for crystalline GST-225 [39,40], as well as with the calculated values for the recrystallized models studied here. The IPR analysis indicates very weak (or no) localization for the tail electronic states at the bottom of the conduction band and the top of the valence band of the SQS model structure. The low degree of spatial localization of the LUMO state can be associated with the absence of homopolar bonds (and hence of antisite defects) in the SQS structure, compared to the recrystallized GST-225 configurations *M1* (see Fig. 1) and *M2* (see Fig. 2), for example. A visualization of the HOMO (highest occupied molecular orbital) electronic state for the SQS model is also shown in Fig. 4 (right). Te atoms next to vacancylike regions within the simulated structure are associated with the weak spatial localization of the electronic state at the top of the valence band in the periodic cell of the SQS model.

We note that a distinct vacancy-cluster-induced localization for the electronic states at the top of the valence band, similar to that previously reported by DFT-based simulations [24], was not observed for the recrystallized model structures (*M1*–*M6*) studied here. Visualization of the molecular orbital for the HOMO in model *M6* (Fig. S4 in [37]), with no imposed structural constraints throughout the crystallization simulation, shows that the localization of the electronic state is associated with an amorphouslike region which is part of a crystalline-amorphous grain boundary in the final recrystallized configuration of this model structure. This highlights the significant effect of the compositional (and structural)

disorder on the spatial localization of the electronic states at the band edges of the recrystallized models.

B. Evolution of electronic structure

The time evolution of the electronic structure during the crystallization simulation was investigated for the GST-225 model *M5*. Nine configurations along the DFT-MD crystallization trajectory were selected, at 0 (initial), 2.2, 3.4, 4.2, 4.6, 5.0, 5.4, 5.7, and 7.1 ns (final), and the electronic structure was calculated by performing a geometry-optimization simulation, for each of them, with hybrid-DFT. The evolution of the total DOS together with the IPR spectrum of the electronic states near the valence- and conduction-band edges for the simulated structure *M5* is shown in Fig. 5. The initial amorphous GST-225 model exhibits a KS band gap of 0.65 eV, which is in accordance with the experimentally reported values, ranging between 0.6 and 0.8 eV [39,40], as well as with previous modeling studies [36,52]. The IPR analysis shows that there are localized electronic states at the bottom of the conduction band, while some partially localized tail states appear at the top of the valence band of this amorphous model structure. We note that such behavior is typical for a glassy material and it is in agreement with previous simulation studies in amorphous GST-225 [18,20]. During the crystallization simulation, defect electronic states arise inside the band gap of the modeled system, which can disappear and reappear, in a random fashion, as the simulation progresses. In addition, it can be observed that the degree of spatial localization of the electronic states around the Fermi level fluctuates along the MD trajectory.

A well-defined strongly localized in-gap state emerges in the electronic structure of the modeled system at 2.2 ns after the beginning of the simulation, while in a snapshot at 3.4 ns there is no such defect in the band gap. The electronic-structure calculation for the configuration at $t = 5$ ns shows a deep unoccupied electronic state, at 0.1 eV above the valence-band maximum. In a snapshot shortly after this (at 5.4 ns), a group of three unoccupied electronic states appear in the band gap, next to each other, which then disappear quickly (at 5.7 ns), leaving one such (rather delocalized) defect state in the electronic structure. Also, in the end of this crystallization simulation, the final recrystallized GST-225 model structure exhibits a localized deep defect state, which is an unoccupied electronic state located very close to the top of the valence band.

The molecular orbital and atomic structure of the deep unoccupied defect state identified in the final recrystallized configuration of the GST-225 model *M5* is shown in Fig. 6 (top). Sb-Sb homopolar bonds from two different, four- and three-coordinated, Sb atoms are associated with the spatial localization of the electronic state. The formation of Ge(Sb)-Te-Ge(Sb)-Te fourfold rings leads to the creation of a cubic structural motif within the defect environment, with two six-coordinated Ge atoms being members of this cube.

For the GST-225 configuration at $t = 2.2$ ns after the beginning of the crystallization simulation of model *M5*, the hybrid-DFT electronic-structure calculation revealed the formation of a (transient) localized electronic state inside the band gap. The unoccupied in-gap defect state is located at an
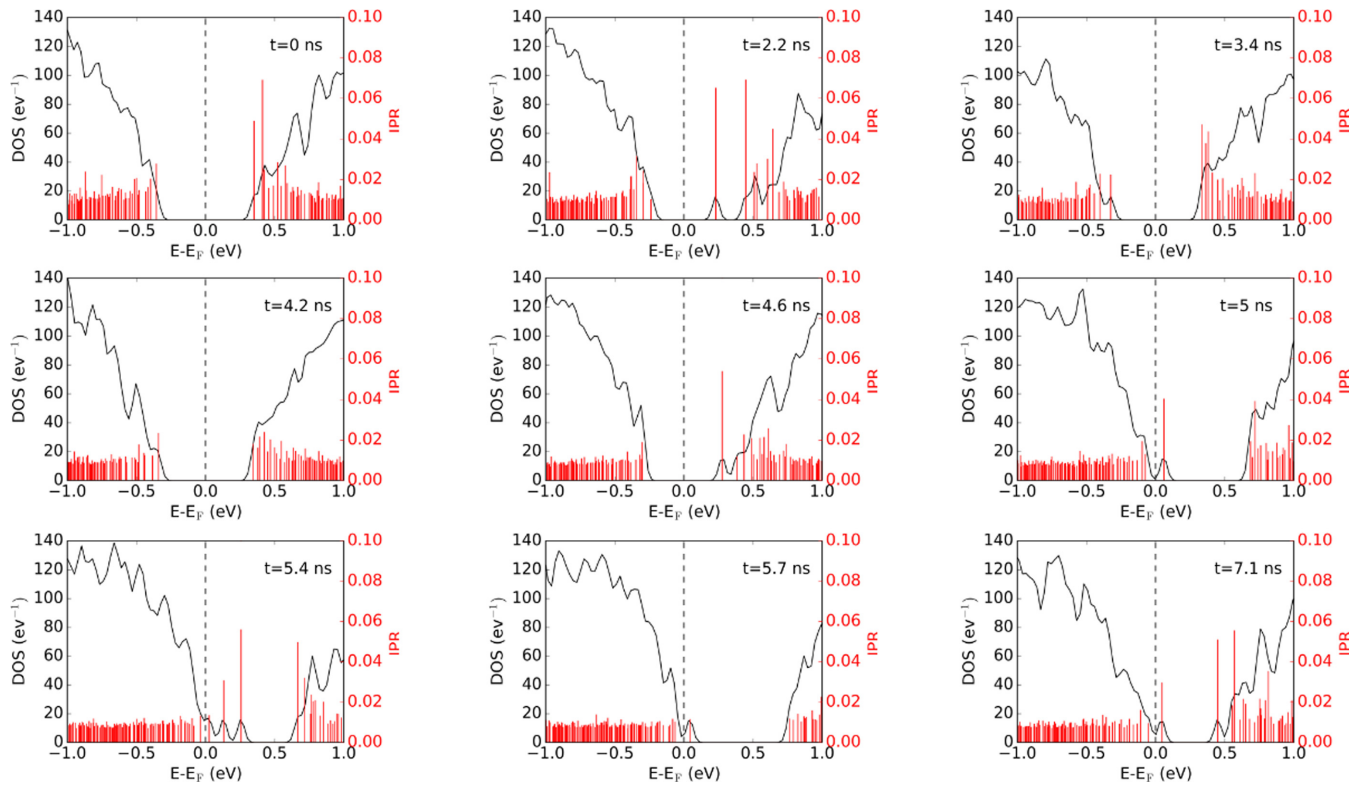
FIG. 5. Total electronic densities of states (DOS, black solid line) near the top of the valence band and the bottom of the conduction band for nine configurations, at different times along the molecular-dynamics trajectory, from the crystallization simulation of the GST-225 model *M5*. The corresponding values of the inverse participation ratio (IPR) for the Kohn-Sham orbitals are highlighted with red spikes, in every case.

energy level of 0.23 eV below the bottom of the conduction band, with the calculated band gap being 0.69 eV for this snapshot of the simulated structure. The molecular orbital associated with this in-gap electronic state, formed during the simulation of model *M5*, is shown in Fig. 6 (bottom). Three Ge atoms, one five-coordinated, one four-coordinated (in a tetrahedral configuration and with a Ge-Ge bond), and one three-coordinated, create the local atomic environment in which the defect state is localized in the simulated structure. In addition, a Ge-Te-Ge-Te fourfold ring connected to another fivefold ring contribute to the picture of the host structural motif for the localized electronic state. Midgap defect electronic states have been previously identified and characterized in melt-quenched models of amorphous GST-225, where it was demonstrated that crystallinelike atomic fragments within the glassy network, consisting of groups of high-coordination Ge atoms and fourfold ring structures are the local atomic environments that are mostly responsible for hosting the localized midgap electronic states inside the simulated glass [20,22].

Calculation of the Bader ionic charges can provide some information on the evolution of the atomic geometry during the crystallization event. The time evolutions of the average Bader charges for Ge, Sb, and Te atoms are shown in Fig. 7 for the nine selected configurations, at different times, along the crystallization trajectory of GST-225 model *M5*. A systematic increase of the average Bader-charge values for Ge and Sb atoms, from $0.25e$ to $0.41e$ and from $0.39e$ to $0.56e$, respectively, was identified as the simulation progresses from the initial amorphous model ($t = 0$ ns) to the final recrystallized

structure ($t = 7.1$ ns), whereas a simultaneous decrease of the corresponding value, from $-0.25e$ to $-0.39e$, was revealed for Te atom. These trends in the time evolution of the calculated Bader charges for the atomic species of model *M5* are indicative of the transition from a glassy to a crystallinelike structure during the crystallization simulation.

C. Similarity of recrystallized structures

The similarity relationships between the initial GST-225 amorphous model and the obtained recrystallized structures from all the different crystallization simulations can be established, at a glance, through the construction of a configurational map [53]. This can be achieved by using an informative representation for the configuration of each model structure together with a suitable dimensionality reduction technique [54]. In this study, a multispecies, global, smooth overlap of atomic positions (SOAP) descriptor [55] was employed to represent each simulated structure, while multidimensional scaling (MDS) has been adopted as the embedding technique [56,57].

Each SOAP descriptor is a vector (**q**) existing in a high-dimensional space, while a measurement of the similarity between two atomic environments is given by the dot product of these vectors [53,55]. SOAP descriptors are normalized such that the dot product of any two of them lies between 0, corresponding to no similarity whatsoever, and 1, corresponding to two identical local environments. Based on this information, for two simulated recrystallized geometries α

FIG. 7. Time evolution of average Bader charges for every type of atom during the crystallization simulation of the GST-225 model *M5*.
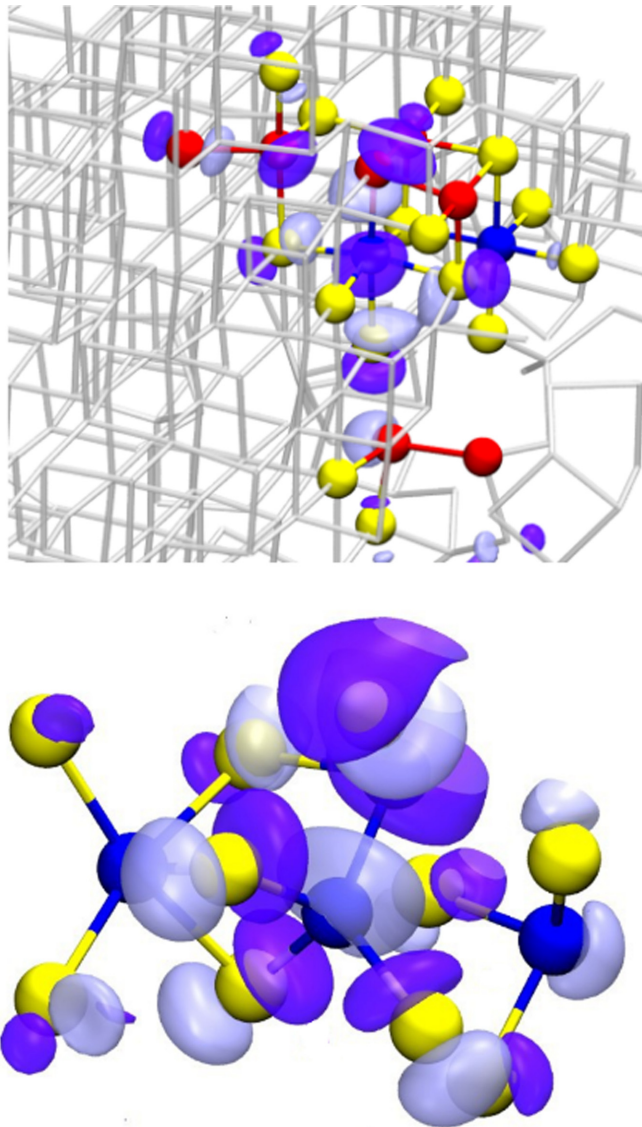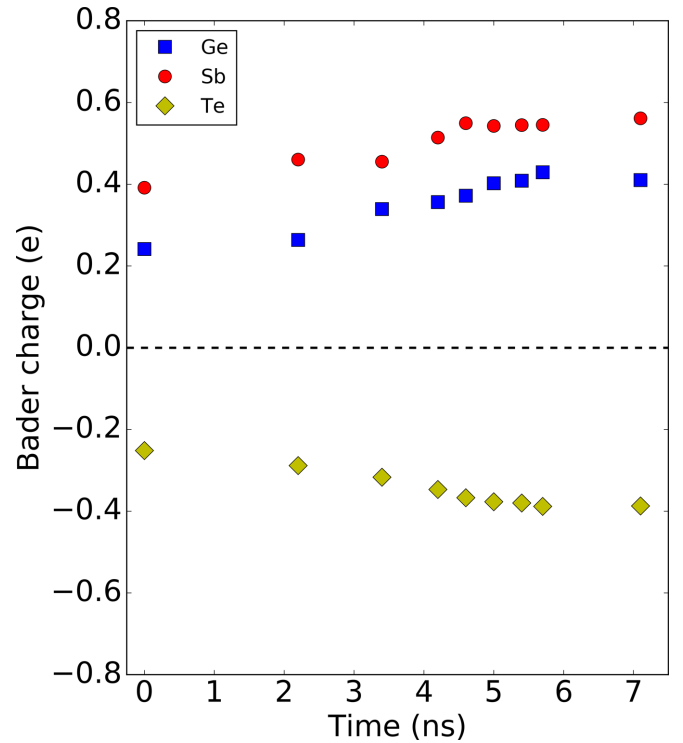

FIG. 6. Top panel: Atomic geometry and molecular orbital of the deep unoccupied electronic state (located at an energy level of 0.1 eV above the top of the valence band) identified in the configuration at the end (7.1 ns) of the crystallization simulation of the GST-225 model *M5*. Bottom panel: Local atomic structure and molecular orbital of the defect electronic state (located at 0.23 eV below the conduction-band minimum) identified inside the band gap at 2.2 ns after the beginning of the crystallization simulation for the GST-225 model *M5*. In both panels, color codes and representations for atomic species, bonds, and isosurfaces as in Fig. 1.

and β, a configurational distance (similarity) metric was constructed as

$$d_{\alpha\beta} = \sqrt{2 - 2\langle \mathbf{q}_\alpha, \mathbf{q}_\beta \rangle},$$

where $\langle \mathbf{q}_\alpha, \mathbf{q}_\beta \rangle$ is the dot product of the corresponding SOAP descriptors.

MDS is a nonlinear dimensionality-reduction technique that takes distances as input and can thus be used to visualize the SOAP data in a two-dimensional (2D) space. For all the indexed model structures the MDS approach constructs embedding vectors (**e**), that have an Euclidean distance that is as

close as possible to the high-dimensional (SOAP-based) distance metric we defined above, by performing a least-squares minimization of the stress function (σ), calculated as

$$\sigma(\mathbf{q}_\alpha, \mathbf{q}_\beta) = \sqrt{\frac{\sum_{\alpha \neq \beta} (d_{\alpha\beta} - ||\mathbf{e}_\alpha - \mathbf{e}_\beta||)^2}{\sum_{\alpha \neq \beta} d_{\alpha\beta}^2}},$$

where $d_{\alpha\beta}$ is the SOAP distance between the α and β configurations in the high-dimensional space, and $||\mathbf{e}_\alpha - \mathbf{e}_\beta||$ is the distance of the corresponding embedding vectors in the reduced (in our case 2D) representation. The final value of the stress reflects the quality of the representation for all the produced data points; the stress is zero if the original distances are completely maintained. For the data set of the recrystallized structures analyzed in this study, a stress value of 0.028 was obtained, corresponding to an excellent embedding. We note that the MDS implementation available in the SCIKIT-LEARN library [58] was employed here.

Hence, in that way, the high-dimensional SOAP data can be embedded into 2D maps in which they can be interpreted accordingly [59,60]. We note that the MDS coordinates have arbitrary units; nevertheless, the distances between points on the respective map reliably reflect the (dis)similarity of configurations in their high-dimensional space. The MDS 2D map that is constructed based on the hybrid-DFT geometry-optimization calculations of the six recrystallized GST-225 structures (models *M1* to *M6*), the SQS-generated model, and the initial (melt-quenched, MQ) glassy structure is shown in Fig. 8. The hexagonal crystalline structure of GST-225 (Kooi
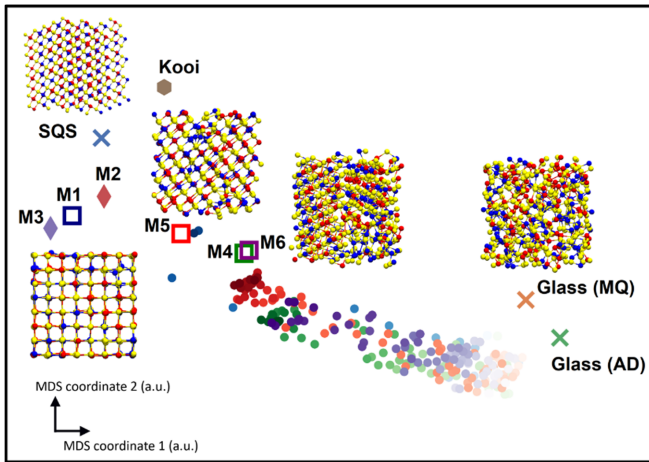
FIG. 8. A two-dimensional SOAP-based similarity map for amorphous (MQ and AD), crystalline (cubic SQS and hexagonal Kooi), and recrystallized structures (during crystallization and final models of *M1*, *M2*, *M3*, *M4*, *M5*, and *M6*) of GST-225. The plot includes configurations from the recrystallization simulations and the SQS-generated structure. The visualization is based on a structural dissimilarity (distance) metric using the SOAP kernel and on embedding by multidimensional scaling (MDS). The closer two points are on the map, the more similar the corresponding structures, and vice versa. Different symbols and color schemes are used for the various simulated structures. Atomic geometries of relevant structural models are shown in the map, where Ge atoms are blue, Sb are red, and Te are yellow.

structure) [13] and an as-deposited-generated (AD) amorphous structure [61], both optimized with hybrid-DFT, have been used as reference points in the 2D map. In addition, raw data (220 configurations) from the DFT-MD crystallization trajectories of the different simulations previously performed were added in the map to investigate the evolution of the GST-225 structure during crystallization [9–11].

In the 2D space of Fig. 8, structures that are similar appear close together, whereas structures that are dissimilar are further apart; therefore, data points that are close to each other on the map indicate close similarity between the model structures, from the point of view of the configurational descriptor [53]. It can be observed that the glassy structures (MQ and AD) are clearly separated from the final recrystallized models, the SQS and the Kooi crystalline structures. Moreover, the cubic rock-salt-like recrystallized structures are distinguished from the hexagonal crystalline phase of GST-225. Walking through the map from right to left, the selected configurations from the (different) crystallization trajectories roughly align with the path that connects the initial amorphous structure to the SQS model of the cubic phase. The existence of homopolar bonds in the recrystallized structures, compared to the SQS structure, can explain the variations from a potential perfect alignment. The final recrystallized structures of GST-225 models *M1* (600 K, ordered history, not fixed), *M2* (600 K, ordered history, fixed), and *M3* (700 K, ordered history, fixed) were found to be very close in the MDS map, highlighting a close similarity between the obtained model structures from these crystallization simulations, while model *M2* appears to be the most similar to the SQS cubic structure. The data points

TABLE I. Average Bader charges (in e) of the atomic species and calculated cohesive energies (E_{coh} in eV/atom) for all the different final recrystallized GST-225 model structures studied here, the SQS-generated and the Kooi crystalline structures.

| Model | Bader charge | | | E_{coh} |
	Ge	Sb	Te	
M1	0.47	0.62	−0.43	−3.670
M2	0.47	0.60	−0.42	−3.663
M3	0.50	0.61	−0.44	−3.669
M4	0.42	0.58	−0.40	−3.657
M5	0.41	0.56	−0.39	−3.659
M6	0.41	0.56	−0.39	−3.655
SQS	0.53	0.64	−0.47	−3.807
Kooi	0.57	0.69	−0.50	−3.869

for the final recrystallized structures of models *M4*, *M5*, and *M6*, obtained from the simulations at 600 K with no ordered history, are further away from the recrystallized structures of models *M1*, *M2*, and *M3*, and the SQS model. This indicates that these crystallization simulations led to the formation of more disordered structures, revealing as well their partially crystallized character.

The structural dissimilarity between the group of the final recrystallized models *M1*, *M2*, and *M3*, and the group of the final recrystallized models *M4*, *M5*, and *M6* is also reflected on the Bader ionic charges and the cohesive energies of the simulated structures, shown in Table I. The computed values of the average Bader charges for Ge and Sb atoms are higher for the recrystallized structures of the first group compared to the respective values for the models of the second group, while for Te atoms the average Bader charges are lower in the first group than those in the second group. In addition, a similar trend can be observed for the calculated cohesive energies, which are consistently lower for the models of the first group. Such differences indicate that the GST-225 model structures *M1*, *M2*, and *M3* are *more crystalline* compared to the structures of models *M4*, *M5*, and *M6*, which have a more disorderlike atomic geometry in their final recrystallized configurations. We note that this observation is in agreement with the findings reported in Ref. [10], where the presence of multiple crystallites was identified in the final recrystallized structure of GST-225 model *M4*, while the formation of a grain boundary occurred in the crystallization event related to model *M6*, for example.

IV. SUMMARY AND CONCLUSIONS

Hybrid-DFT calculations were employed to optimize the geometry of selected recrystallized configurations of the GST-225 PCM material, generated from previous DFT-MD simulations, and to calculate their electronic structures for identifying the nature of the spatial localization of the electronic states in the conduction band. The calculations show that defect-related electronic states are present in the bottom of the conduction band of the GST-225 recrystallized structures. Our analysis demonstrates that Te-Te homopolar bonds are associated with the structural pattern that is involved in

the spatial localization of the conduction-band-edge states, highlighting the impact of Te antisite defects. In principle, the existence of homopolar bonds induces the compositional disorder of the recrystallized structure, leading to an induced spatial localization of the unoccupied electronic states. The very weak localization observed for the conduction-band-minimum electronic state in the antisite-defect free SQS-generated model of GST-225 highlights further the significant role of the Te antisite defects in the character of electron localization for the electronic states at the bottom of the conduction band in the crystalline state of GST-225. In addition, the results show that Sb-Te chain structures across the simulation cell can host localized electronic states in the bottom of the conduction band, indicating that various atomic defective environments can contribute to the electron localization in recrystallized GST-225 models. We note that similar observations have been also recently reported in a recrystallized model structure of $Ge_1Sb_2Te_4$ [27].

It should be noted that the conduction-band-edge electronic states of the recrystallized models studied here show a spatial localization extended in one direction of the simulation cell. However, in principle, strongly localized states, associated with Anderson localization, are characterized by an exponential localization in all directions. This difference probably stems from finite-size effects in our modeled structures; therefore, larger atomistic models are necessary for studying Anderson localization.

Following the evolution of the electronic structure during a crystallization event, the emergence of additional unoccupied electronic states in the band gap was unraveled, while the degree of spatial localization of these defect states varies for different configurations along the crystallization trajectory. Even though the formation of in-gap states in the electronic structure of the modeled system is characterized by a randomness, two very interesting observations related to the structural patterns that host some of them are as follows: (a) tetrahedral, overcoordinated, and undercoordinated Ge atoms, as well as fourfold rings are the local atomic environments associated with the generation of a shallow localized state below the bottom of the conduction band; and (b) the presence of Sb-Sb homopolar bonds within the defect environment for a deep localized state in the band gap, located very close to the top of the valence band.

An atom-density-based similarity metric (SOAP descriptor) was utilized to examine the degree of structural similarity between the simulated configurations studied here, and by visualization in a 2D map. The crystallization events in which a cubic crystalline seed was initially inserted in the simulation box (and then either kept fixed or not during the crystallization process) led to the generation of recrystallized GST-225 structures with a more crystalline nature, which also had the closest resemblance to the SQS cubic crystalline model structure. In contrast, the recrystallized structures obtained from the crystallization events with no initial imposed structural constraints show a less crystalline character in their final recrystallized geometries. These observations highlight the stochasticity of the transition from the amorphous state to the crystalline state in PCM materials. In addition, they suggest that the timescale and system size accessible within the DFT-MD simulations may be limited for capturing a complete picture of the phase-change process.

The changes in electronic structure during recrystallization of amorphous PCM materials are crucial for the application of these materials in rewritable optical-data storage and nonvolatile electronic memories. Localized electronic states are predicted to be present at the conduction- and valence-band-edges of the recrystallized structures, while various forms of disorder can contribute to the induced spatial localization. Controlling the distribution of localized defect states by tailoring the degree of disorder in the crystalline state of PCM materials can lead to the realization of multilevel storage operation in future nonvolatile PCRAM devices.

[1] S. Raoux, W. Wełnic, and D. Ielmini, Chem. Rev. **110**, 240 (2010).

[2] P. Noé, C. Vallée, F. Hippert, F. Fillot, and J.-Y. Raty, Semicond. Sci. Technol. **33**, 013002 (2017).

[3] J.-J. Wang, Y.-Z. Xu, R. Mazzarello, M. Wuttig, and W. Zhang, Materials **10**, 862 (2017).

[4] N. Yamada and T. Matsunaga, J. Appl. Phys. **88**, 7020 (2000).

[5] T. Matsunaga and N. Yamada, Phys. Rev. B **69**, 104111 (2004).

[6] U. Ross, A. Lotnyk, E. Thelander, and B. Rauschenbach, Appl. Phys. Lett. **104**, 121904 (2014).

[7] B. Zhang, W. Zhang, Z. Shen, Y. Chen, J. Li, S. Zhang, Z. Zhang, M. Wuttig, R. Mazzarello, E. Ma, and X. Han, Appl. Phys. Lett. **108**, 191902 (2016).

[8] T. H. Lee and S. R. Elliott, Phys. Rev. Lett. **107**, 145702 (2011).

[9] J. Kalikka, J. Akola, J. Larrucea, and R. O. Jones, Phys. Rev. B **86**, 144113 (2012).

[10] J. Kalikka, J. Akola, and R. O. Jones, Phys. Rev. B **94**, 134105 (2016).

[11] J. Kalikka, J. Akola, and R. O. Jones, Phys. Rev. B **90**, 184109 (2014).

[12] I. Ronneberger, W. Zhang, H. Eshet, and R. Mazzarello, Adv. Funct. Mater. **25**, 6407 (2015).

[13] B. J. Kooi and J. T. M. De Hosson, J. Appl. Phys. **92**, 3584 (2002).

[14] B. J. Kooi, W. M. G. Groot, and J. T. M. De Hosson, J. Appl. Phys. **95**, 924 (2004).

[15] J. L. F. Da Silva, A. Walsh, and H. Lee, Phys. Rev. B **78**, 224111 (2008).

[16] N. F. Mott, E. A. Davis, and R. A. Street, Philos. Mag. **32**, 961 (1975).

[17] J. Luckas, D. Krebs, S. Grothe, J. Klomfaß, R. Carius, C. Longeaud, and M. Wuttig, J. Mater. Res. **28**, 1139 (2013).

[18] S. Caravati, M. Bernasconi, T. D. Kühne, M. Krack, and M. Parrinello, J. Phys.: Condens. Matter **21**, 255501 (2009).

[19] F. Zipoli, D. Krebs, and A. Curioni, Phys. Rev. B **93**, 115201 (2016).

[20] K. Konstantinou, F. C. Mocanu, T. H. Lee, and S. R. Elliott, Nat. Commun. **10**, 3065 (2019).

[21] F. C. Mocanu, K. Konstantinou, J. Mavračić, and S. R. Elliott, Phys. Status Solidi RRL **15**, 2000485 (2021).

[22] K. Konstantinou, F. C. Mocanu, J. Akola, and S. R. Elliott, Acta Mater. **223**, 117465 (2022).

[23] T. Siegrist, P. Jost, H. Volker, M. Woda, P. Merkelbach, C. Schlockermann, and M. Wuttig, Nat. Mater. **10**, 202 (2011).

[24] W. Zhang, A. Thiess, P. Zalden, P. H. Zeller, R. Dederichs, J.-Y. Raty, M. Wuttig, S. Blügel, and R. Mazzarello, Nat. Mater. **11**, 952 (2012).

[25] J. M. Skelton, D. Loke, T. H. Lee, and S. R. Elliott, Phys. Status Solidi B **250**, 968 (2013).

[26] M. Xu, W. Zhang, R. Mazzarello, and M. Wuttig, Adv. Sci. **2**, 1500117 (2015).

[27] Y. Xu, Y. Zhou, X.-D. Wang, W. Zhang, E. Ma, V. L. Deringer, and R. Mazzarello, Adv. Mater. **34**, 2109139 (2022).

[28] A. Zunger, S.-H. Wei, L. G. Ferreira, and J. E. Bernard, Phys. Rev. Lett. **65**, 353 (1990).

[29] A. van de Walle, P. Tiwary, M. de Jong, D. L. Olmsted, M. Asta, A. Dick, D. Shin, Y. Wang, L. Q. Chen, and Z. K. Liu, CALPHAD **42**, 13 (2013).

[30] M. Ångqvist, W. A. Muñoz, J. M. Rahm, E. Fransson, C. Durniak, P. Rozyczko, T. H. Rod, and P. Erhart, Adv. Theory Simul. **2**, 1900015 (2019).

[31] J. VandeVondele, M. Krack, F. Mohamed, M. Parrinelo, T. Chassaing, and J. Hutter, Comput. Phys. Commun. **167**, 103 (2005).

[32] G. Lippert, J. Hutter, and M. Parrinello, Mol. Phys. **92**, 477 (1997).

[33] J. VandeVondele and J. Hutter, J. Chem. Phys. **127**, 114105 (2007).

[34] S. Goedecker, M. Teter, and J. Hutter, Phys. Rev. B **54**, 1703 (1996).

[35] M. Guidon, J. Hutter, and J. VandeVondele, J. Chem. Theory Comput. **5**, 3010 (2009).

[36] K. Konstantinou, S. R. Elliott, and J. Akola, J. Mater. Chem. C **10**, 6744 (2022).

[37] See Supplemental Material at http://link.aps.org/supplemental/10.1103/PhysRevB.106.184103 for a comparison of obtained electronic properties (DOS and IPR) between a GGA (PBE) and a hybrid-functional (PBE0) geometry-optimization calculation, and a visualization of the molecular orbital and atomic structure of the HOMO electronic state in the recrystallized GST-225 model M6.

[38] M. Guidon, J. Hutter, and J. VandeVondele, J. Chem. Theory Comput. **6**, 2348 (2010).

[39] B. S. Lee, J. R. Abelson, S. G. Bishop, D. H. Kang, B. K. Cheong, and K. B. Kim, J. Appl. Phys. **97**, 093509 (2005).

[40] T. Kato and K. Tanaka, Jpn. J. Appl. Phys. **44**, 7340 (2005).

[41] J. Dong and D. A. Drabold, Phys. Rev. B **54**, 10284 (1996).

[42] R. Mazzarello, S. Caravati, S. Angioletti-Uberti, M. Bernasconi, and M. Parrinello, Phys. Rev. Lett. **104**, 085503 (2010).

[43] K. Konstantinou, F. C. Mocanu, T. H. Lee, and S. R. Elliott, J. Phys.: Condens. Matter **30**, 455401 (2018).

[44] A. D. Becke and K. E. Edgecombe, J. Chem. Phys. **92**, 5397 (1990).

[45] T. H. Lee and S. R. Elliott, Adv. Mater. **29**, 1700814 (2017).

[46] T. H. Lee and S. R. Elliott, Adv. Mater. **32**, 2000340 (2020).

[47] Z. Sun, J. Zhou, H. K. Mao, and R. Ahuja, Proc. Natl. Acad. Sci. USA **109**, 5948 (2012).

[48] G. Hua and D. Li, Phys. Chem. Chem. Phys. **18**, 4753 (2016).

[49] Y. Cheng, L. Zhu, G. Wang, J. Zhou, S. R. Elliott, and Z. Sun, Comput. Mater. Sci. **183**, 109803 (2020).

[50] A. Savin, R. Nesper, S. Wengert, and T. F. Fässler, Angew. Chem., Int. Ed. Engl. **36**, 1808 (1997).

[51] G. Henkelman, A. Arnaldsson, and H. Jónsson, Comput. Mater. Sci. **36**, 354 (2006).

[52] K. Konstantinou, T. H. Lee, F. C. Mocanu, and S. R. Elliott, Proc. Natl. Acad. Sci. USA **115**, 5353 (2018).

[53] S. De, A. P. Bartók, G. Csányi, and M. Ceriotti, Phys. Chem. Chem. Phys. **18**, 13754 (2016).

[54] B. Cheng, R.-R. Griffiths, S. Wengert, C. Kunkel, T. Stenczel, B. Zhu, V. L. Deringer, N. Bernstein, J. T. Margraf, K. Reuter, and G. Csányi, Acc. Chem. Res. **53**, 1981 (2020).

[55] A. P. Bartók, R. Kondor, and G. Csányi, Phys. Rev. B **87**, 219902(E) (2013).

[56] J. B. Kruskal, Psychometrika **29**, 1 (1964).

[57] I. Borg and P. J. F. Groenen, *Modern Multidimensional Scaling: Theory and Applications*, 2nd ed., Springer Series in Statistics (Springer, New York, 2005).

[58] F. Pedregosa, G. Varoquaux, A. Gramfort, V. Michel, B. Thirion, O. Grisel, M. Blondel, P. Prettenhofer, R. Weiss, V. Dubourg, J. Vanderplas, A. Passos, D. Cournapeau, M. Brucher, M. Perrot and E. Duchesnay, J. Mach. Learn. Res. **12**, 2825 (2011).

[59] J. Mavračić, F. C. Mocanu, V. L. Deringer, G. Csányi, and S. R. Elliott, J. Phys. Chem. Lett. **9**, 2985 (2018).

[60] T. C. Nicholas, A. L. Goodwin, and V. L. Deringer, Chem. Sci. **11**, 12580 (2020).

[61] J. Akola, J. Larrucea, and R. O. Jones, Phys. Rev. B **83**, 094113 (2011).